Journal of Materials Chemistry A

PAPER

Cite this: J. Mater. Chem. A, 2015, 3, 9517

Facile synthesis of Pd nanostructures in hexagonal mesophases as a promising electrocatalyst for ethanol oxidation†

Srabanti Ghosh,*[ab] Hynd Remita,[bc] Prasenjit Kar,[a] Susobhan Choudhury,[a] Samim Sardar,[a] Patricia Beaunier,[d] Partha Sarathi Roy,[e] Swapan Kumar Bhattacharya[e] and Samir Kumar Pal[a]

Received 4th February 2015
Accepted 16th March 2015

DOI: 10.1039/c5ta00923e

www.rsc.org/MaterialsA

One of the significant challenges for the commercialization of direct ethanol fuel cells (DEFCs) is the preparation of active, robust, and low-cost catalysts. In this work, a facile and reproducible method is demonstrated for the synthesis of Pd assembled nanostructures in a hexagonal mesophase formed by a quaternary system (Pd-doped water, surfactant, oil, and cosurfactant) *via* photoirradiation. The formation of Pd nanostructures in the confined region of hexagonal mesophases was further supported by water relaxation dynamics study using a solvation probe. The mesophases can be doped with high concentrations of a palladium salt (0.1 M) without any disturbance to the structure of the mesophases which results in a high yield and facilitates the clean synthesis of Pd nanostructures without using any toxic chemicals. Electrochemical measurement confirms that the as-prepared catalysts exhibit significant electrocatalytic activity for ethanol oxidation in alkaline solution. Additionally, we present an alternative strategy using reduced graphene oxide nanosheets in combination with Nafion (a proton conducting phase) as a support, revealing the pronounced impact on dramatically enhanced electrocatalytic activity and stability of Pd nanostructures compared to Nafion alone. This unique combination allowed the effective dispersion of the Pd nanostructures that is responsible for the enhancement of the catalytic activity. Our approach paves the way towards the rational design of practically relevant catalysts with both enhanced activity and durability for fuel cell applications.

1. Introduction

The development of advanced materials and processes is a central issue which leads to the ultimate goal of accelerating the implementation of novel nanomaterials-based technology providing clean and affordable energy.[1–3] Platinum is the superlative electrocatalyst for most of the relevant reactions involved in fuel cells which constitute promising future power sources. However, several critical issues such as migration, aggregation and dissolution in harsh electrochemical environments as well as the weak tolerance to CO poisoning and the high cost must be resolved before Pt-based electrocatalysts can be commercialized.[4,5] Alternatively, Pd based nanostructured materials play a crucial role in the catalysis of various relevant reactions in fuel cells, resulting in enhanced intrinsic electroactivity with high energy conversion efficiency, which is suitable for direct ethanol fuel cells (DEFCs).[6–8] Therefore, many recent efforts have been devoted to control the morphology and composition of Pd-based catalysts that can offer a great opportunity to achieve enhanced catalytic performance and higher utilization of Pd.[9–14] In our earlier reports, Pd nanowires, and porous Pd nanoballs connected with three-dimensional Pd nanowires demonstrated superior electro-catalytic activity for ethanol oxidation and appear as promising candidates for fuel cell applications.[15,16] In spite of these successful demonstrations, it is important to note that their mass activity (in terms of Pd) for ethanol electrooxidation is still not satisfactory.[17–19] Hence, it is highly desirable to develop a simple method for the synthesis of novel Pd nanoparticles (NPs) based electrocatalysts with high activity and durability for fuel cell applications. Moreover, various shape-controlled Pd nanostructures have been extensively explored for electrocatalysis. Nevertheless, reports regarding self-assembled Pd nanostructures are scarce. Herein, we demonstrate a very

[a]Department of Chemical, Biological and Macromolecular Sciences, S. N. Bose National Centre for Basic Sciences, Block JD, Sector III, Salt Lake, Kolkata 700 098, India. E-mail: ghosh.srabanti@mail.com; srabanti.ghosh@bose.res.in

[b]Laboratoire de Chimie Physique, UMR 8000-CNRS, Université Paris-Sud, 91405 Orsay Cedex, France

[c]CNRS, Laboratoire de Chimie Physique, UMR 8000, 91405 Orsay, France

[d]Sorbonne Universités, UPMC Univ. Paris 06, UMR 7197-CNRS, Laboratoire de Réactivité de Surface, F-75005 Paris, France

[e]Physical Chemistry Section, Department of Chemistry, Jadavpur University, 700 032, Kolkata, India

† Electronic supplementary information (ESI) available: Additional information, polarized light micrographs, FTIR spectra, TEM and HRTEM images and CV pattern. See DOI: 10.1039/c5ta00923e

simple and efficient route to synthesize Pd nanostructures in liquid crystals by photoreduction.

A liquid crystal (LC) appears as a perfect candidate for the matrix-guided synthesis and self-assembly of nanoscale materials as it combines order and mobility at the molecular (nanoscale) level.[20–23] Few examples have been reported for the preparation of nanostructures in nematic LCs as structure-directing templates.[22,24] One of the significant problems associated with templating of nematic domains is that nanoparticles are expelled to domain boundaries which leads to the formation of particulate networks and consequently, free-standing porous materials cannot be obtained using this route.[25–27] Attard *et al.* successfully demonstrated that direct hexagonal LCs prepared using a ternary mixture (nonionic surfactant, metal salts, and water) can be used as a template for the synthesis of bulk porous materials and porous metal films by electro-deposition.[28,29] Recently, we reported a systematic study of the effect of the templating approach allowing the synthesis of bimetallic nanoballs of tunable porosity and composition in a swollen hexagonal mesophase (SLC).[30] The swollen mesophases consist of surfactant-stabilized oil-swollen tubes that are arranged on a triangular lattice in an aqueous medium.[31,32] In the past years, we employed doped SLC with various compounds and used them as nanoreactors to synthesize diverse nanostructured materials (such as metals, polymers or oxides) both in the aqueous and in the oil phases.[33–36] Here, the photoreduction of the palladium salt is induced by UV light irradiation within the aqueous phase of hexagonal mesophases. By virtue of employing Pd as an active electrocatalyst, we studied the ethanol oxidation reaction (EOR) using as-prepared Pd nanostructures as the anode material. Additionally, in order to enhance the dispersion and accessibility of the catalyst, a reduced graphene oxide nanosheets (RGO) modified Pd nanostructure has been used in combination with a Nafion support during electrooxidation.

Despite the immense advances in unsupported nanostructured noble metals as electrocatalysts, the relatively low efficiency and high usage of noble metals in such unsupported metal catalysts still limit their practical applications. Hence, the design and fabrication of more active electrocatalysts with excellent performance, durability and low cost are of great importance. To improve the electrochemical performance of these catalysts, carbon based conductive substrates such as carbon nanotubes (CNTs), carbon fibers and Vulcan XC-72 (VXC) are widely used as supports to disperse the metal NPs.[37–40] Supported metal NPs play a pivotal role as catalysts for energy storage/conversion; however, the aggregation tendency of NPs is an impediment for stable performance and loss of active surface area is a major cause of deactivation for supported catalysts.[41,42] Recently, we demonstrated that the utilization of conducting polymer nanostructures improves the electrocatalytic activity and durability of Pd catalysts.[43] A good catalyst support should possess good conductivity and mechanical strength, and long term stability with a high surface area.[44,45] In this respect, graphene oxides possess a high surface area, low cost and enhanced conductivity, and they have been chosen as excellent carbon supports for catalysts to achieve enhanced electrochemical performance for fuel oxidation, oxygen reduction and water splitting reactions.[46–49] The ease of processibility and functionalization makes graphene-based functional materials ideal candidates for a variety of energy applications.[50,51] Hence, reduced RGO nanosheets in combination with Nafion can be used as an efficient support for metal NPs which would exhibit fascinating catalytic properties. We report the synthesis and characterization of assembled palladium nanostructures in hexagonal mesophases. We demonstrate that the Pd nanostructures synthesized in soft templates are promising electrocatalysts having superior activity and stability for EOR. Moreover, the introduction of RGO nanosheets along with Nafion into the electrode containing the Pd nanostructures leads to high electrocatalytic activity and durability for EOR.

2. Experimental

2.1 Reagents

$Pd(NH_3)_4Cl_2$ (99% purity), cetylpyridinium chloride (CPCl, 98% purity), sodium chloride, cyclohexane (>99%), pentanol (≥99%), 5 wt% Nafion solution, coumarin (C500), 4-(dicyanomethylene)-2-methyl-6-(*p*-dimethylamino-styryl)-4*H*-pyran (DCM), graphite powder, 2-propanol and ethanol were purchased from Sigma-Aldrich. All compounds were used as received. Ultrapure water (Millipore System, 18.2 MΩ cm) and ethanol (≥99% for HPLC, purchased from Sigma-Aldrich) were used as solvents.

2.2 Preparation of the catalyst

Swollen hexagonal mesophases with CPCl as the surfactant were prepared following the previously published method with some modifications.[31,35] Typically, 1 g of the surfactant (CPCl) was dissolved in 2 mL of brine (an aqueous solution containing 0.1 mol L^{-1} NaCl or 0.1 mol L^{-1} $Pd(NH_3)_4Cl_2$ in Pyrex glass tubes. After vigorous agitation at 30 °C, the surfactant completely dissolved to give a transparent and viscous micellar solution. The subsequent addition of cyclohexane in the micellar solution under stirring leads to a white unstable emulsion. A cosurfactant, pentanol-1, was added to the mixture, which was then strongly vortexed for a few minutes. This led to a perfectly colorless, translucent, birefringent and stable gel: a hexagonal mesophase. All experiments were performed at room temperature. The doped mesophases with the Pd salt were used as soft templates to synthesize palladium nanostructures induced by UV light irradiation. For *in situ* photoreduction, the doped mesophases were transferred to quartz cells and irradiated with an Oriel 300 W xenon UV-visible lamp at a distance of 5 cm for 12 hours. After the reaction, the metal NPs were easily extracted from the mesophases by a simple washing process with 2-propanol, centrifuged, and washed several times to remove the surfactant, the cosurfactant and the salt. For solvation dynamics study, we doped hexagonal mesophases with two common solvation probes, coumarin (C500) and 4-(dicyanomethylene)-2-methyl-6-(*p*-dimethylamino-styryl)-4*H*-pyran (DCM).

The graphene used here was prepared by the modified Hummers method.[52,53] Firstly, 1 g of graphite, 0.5 g of $NaNO_3$ and 30 mL of H_2SO_4 (98 wt%) were added into a flask with

stirring in an ice bath. Then 3.0 g of $KMnO_4$ was added gradually in one hour. After cooling, the mixture was continually stirred at room temperature for 3 days. The mixture was then slowly added into 100 mL of 5 wt% H_2SO_4 in one hour under stirring. After another two hours of stirring, 2.7 mL of 30 wt% H_2O_2 was added into the mixture and stirred again for two more hours. The mixture was then filtered and washed several times with a solution of 0.5 wt% H_2O_2 and 3 wt% H_2SO_4. Finally, the mixture was washed with distilled water to remove residual metal ions and acid. The product graphene oxide (GO) was dried in air. The GO (mg mL^{-1}) was then dispersed in 2-propanol and exfoliated in an ultrasonic bath followed by deoxygenation under a N_2 flow. The GO sample was then exposed to γ-irradiation at room temperature for 10 h (irradiation dose of 6.4 kGy) under a N_2 atmosphere. The γ-irradiation source, located at Orsay, was a panoramic ^{60}Co gamma-facility of 7000 Curies with a maximum dose rate of 6400 Gy h^{-1}. After the reaction, the reduced GO was centrifuged, and washed several times with ethanol.

2.3 Material characterization

Transmission electron microscopy (TEM) observations were performed using an FEI (Technai S-Twin, operating at 200 kV) instrument and with a JEOL 100CXII transmission electron microscope at an accelerating voltage of 100 kV. Drops of the Pd nanostructures in ethanolic solutions were deposited on carbon coated copper grids and dried under a N_2 flow. XRD patterns were obtained by employing a scanning rate of 0.02° S^{-1} in the 2θ range from 20° to 80° by a PANalytical XPERTPRO diffractometer equipped with Cu Kα radiation (at 40 mA and 40 kV). Optical microscopy of gel samples before and after polymerization was performed with a Leica DMRX polarizing microscope. For optical experiments, the steady-state absorption and emission were determined with a Shimadzu UV-2450 spectrophotometer and a Jobin Yvon Fluoromax-3 fluorimeter, respectively. Picosecond-resolved fluorescence decay transients were measured by using a commercially available spectrophotometer (Life Spec-ps, Edinburgh Instruments, UK) with a 70 ps instrument response function (IRF). The excitation at 375 nm and 409 nm was obtained using pulse laser diodes from PicoQuant, Germany. The observed fluorescence transients were fitted by using a nonlinear least square fitting procedure to a function $\left(X(t) = \int_0^t E(t')R(t-t')\mathrm{d}t'\right)$ comprising of convolution of the IRF ($E(t)$) with a sum of exponential $\left(R(t) = A + \sum_{i=1}^{N} B_i e^{-t/\tau_i}\right)$ with pre-exponential factors (B_i), characteristic lifetimes (τ_i) and a background (A). The relative concentration in a multi-exponential decay was finally expressed as $c_n = \frac{B_n}{\sum_{i=1}^{N} B_i} \times 100$. The quality of the curve fitting was evaluated using reduced chi-square and residual data. It has to be noted that with our time-resolved instrument, we can resolve at least one fourth of the instrument response time constants after the de-convolution of the IRF. The average lifetime (amplitude-weighted) of a multi-exponential decay is expressed as $\tau_{av} = \sum_{i=1}^{N} c_i\tau_i$. Time-resolved emission spectrum (TRES) was used to construct time-dependent fluorescence Stokes shifts.[54,55] The time-dependent fluorescence Stokes shifts, as estimated from TRES, are used to construct the normalized spectral shift correlation function or the solvent correlation function, $C(t)$, defined as, $C(t) = \frac{\nu(t) - \nu(\infty)}{\nu(0) - \nu(\infty)}$, where $\nu(0)$, $\nu(t)$, and $\nu(\infty)$ are the emission maxima (in cm^{-1}) at time 0, t, and ∞ respectively. The $\nu(\infty)$ value corresponds to the emission frequency beyond which it is not significant or no spectral shift is observed. The $C(t)$ function represents the temporal response of the solvent relaxation process. Anisotropy $r(t)$ is defined as $r(t) = \frac{I_{para} - I_{per}}{I_{para} + 2 \times I_{per}}$, where I_{para} is the emission intensity measured parallel to that of excitation and I_{per} is that measured in the perpendicular position. Fourier transform infrared (FTIR) spectra of the solid Pd salt and solid Pd NP powders as synthesized by UV irradiation (obtained after extraction from the mesophases) were recorded using a JASCO FTIR-6300 spectrometer. Scanning wavelengths were varied from 4000 to 600 cm^{-1} with a 2 cm^{-1} spectral resolution with the average of 100 repetition scans for each spectrum.

The Pd content deposited on the electrode (see the next section) was determined by inductively coupled plasma-mass spectrometry (ICP-MS) as follows: (i) the solvent was first evaporated; (ii) samples were mineralized using 5 mL of aqua regia and injected, after 20 times dilution with ultrapure water, *via* a peristaltic pump at 0.1 mL min^{-1} flow rate; (iii) nebulization of samples was performed by means of a micro concentric nebulizer (Micromist); (iv) a 7500 ce ICP-MS (Agilent) was used as the elemental detector. Detection of Pd was performed by selecting an abundant isotope free of interferences, *i.e.*, ^{105}Pd.

2.4 Electrochemical characterization

The electrochemical measurements were conducted at 30 °C in a two compartment glass-cell fitted with a conventional three electrode assembly. In all electrochemical measurements, a glassy carbon rod was used as the working electrode and Hg/HgO/OH (1 M) (designated as MMO) having an equilibrium electrode potential of ~0.1 V with respect to the standard hydrogen electrode (SHE) was used as the reference electrode. A large Pt-foil (1 cm × 1 cm) was used as the counter electrode and potential data were recorded with respect to MMO. Cyclic voltammetric study was performed using a computer aided potentiostat/galvanostat (AEW-2, Munistst, Sycopel Scientific Ltd, UK). The cyclic voltammogram (CV) of each electrode was recorded at the scan rate of 50 mV s^{-1} for several consecutive cycles until a steady profile was obtained. Chronopotentiometry was also performed by applying a current density of 5 mA cm^{-2} with the help of a constant current charger (DB-300, DB Electronics) and the potential was recorded with an EC digital multimeter (DM 610 4B) as described before.[56] The glassy carbon electrode was pretreated using the following process.

First, the surface of the glassy carbon electrode was polished with 1.0, 0.3 and 0.05 μm α-alumina powders in sequence, rinsed thoroughly with twice distilled water and placed in a water-filled ultrasonic bath for a 2 min period. After drying in air, Pd NPs were deposited for further use.

Pd nanostructure suspension consisting of 0.5 mg of Pd NPs in 500 μL of 0.5 wt% Nafion (as Pd/Nafion) and another suspension consisting of 0.25 mg of Pd NPs with 0.25 mg of reduced GO nanosheets (RGO) in 500 μL of 0.5 wt% Nafion (Pd/RGO–Nafion) in ethanol solution were used for the electrochemical characterization. A layer was prepared by depositing 10 μL of the homogeneous solution of Pd NP suspensions on the polished glassy carbon electrode surface.

The above suspensions were used for the determination of the Pd content by ICP-MS and the amount of palladium on the glassy carbon for Nafion and RGO–Nafion was found to be 4.9 μg and 2.48 μg respectively. The layer was allowed to dry for at least 60 min. Pd/RGO–Nafion was not directly deposited on the electrode surface but the Pd nanostructures were embedded within the Nafion and RGO–Nafion matrix.

3. Results and discussion

Swollen hexagonal mesophases, resulting from the surfactant mediated self-assembly in a quaternary system (water, surfactant, cosurfactant, and oil) serve as versatile templates for synthesizing various nanomaterials.[31,35] For Pd nanostructure synthesis, we prepared mesophases doped with a 0.1 M Pd complex with a volume ratio of oil over water (O/W) (v/v) fixed at 1.5 for the *in situ* photoreduction. The Pd nanostructures synthesized in doped CPCl-based mesophases were extracted with 2-propanol. Fig. 1 shows the UV-Vis spectra of the $Pd(NH_3)_4Cl_2$ complex (solid black line) and the suspensions of the Pd nanostructure (solid red line) extracted from mesophases after 12 hours of photoirradiation. The Pd complex shows a peak at 297 nm and after photoirradiation, the intensity of the peak decreases. After the reduction, a new band appears at 258 nm along with a featureless absorption profile in the range of 300–500 nm which indicates the photo-induced reduction of the Pd complex and formation of palladium nanoparticles (Fig. 1).[33] FTIR analysis was also carried out to investigate the chemical structure of the Pd complex before and after photoreduction followed by the Pd nanostructure formation. Fig. S1† illustrates the FTIR spectra of the pure surfactant, the Pd complex and Pd nanostructures after extraction from the mesophases. It appears that the band between 1300 and 1415 cm^{-1} (symmetric type) and in the region 1553–1660 cm^{-1} (antisymmetric type) due to NH_2-deformation and at 825 cm^{-1} ascribed to the rocking modes of NH_3 of the Pd complex which disappeared after photoirradiation also indicate photoreduction of the Pd salt.[57] It is also observed that the bands at 2854 and 2925 cm^{-1} corresponding to the CH_2 stretching modes of the surfactant are absent in the as-prepared Pd nanostructures after template removal.[58] The Pd nanostructure exhibits broad absorption which is consistent with other previously reported Pd based nanostructures.[59,60] Typically, the formation of Pd nanoparticles *via* a chemical or photochemical route is

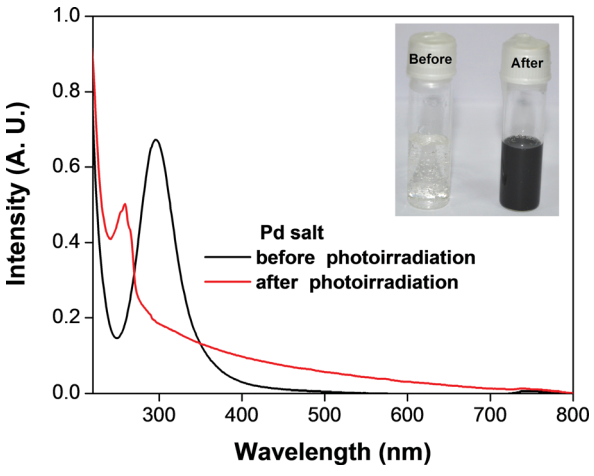

Fig. 1 UV-visible spectra of the $Pd(NH_3)_4Cl_2$ complex before and after photoirradiation. Inset: photographs of hexagonal mesophases doped with 0.1 M $Pd(NH_3)_4Cl_2$ complex before and after UV irradiation exposure. The color change indicates the photoreduction of the Pd complex by UV irradiation.

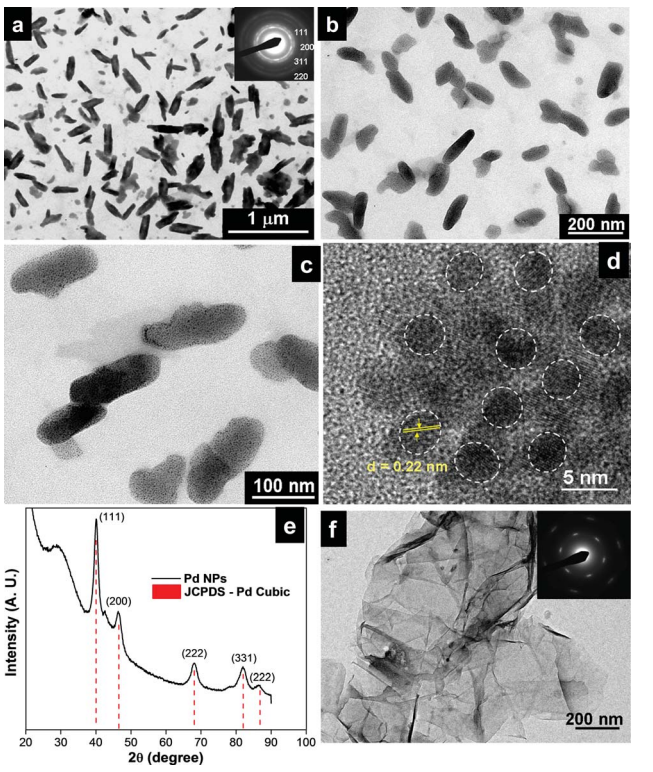

Fig. 2 Transmission electron micrographs of (a–c) Pd nanostructures synthesized in hexagonal mesophases by 12 h UV-irradiation. The inset shows the corresponding indexed SAED pattern. (d) HRTEM high magnification image of palladium nanoparticles. (e) XRD patterns of palladium nanoparticles with JCPDS (05-0681) data. (f) Reduced graphene oxide nanosheets induced by gamma (γ)-irradiation (dose rate: 6.4 kGy h^{-1}, at a dose of 64 kGy) using a solution containing graphene oxides in 2-propanol under a N_2 atmosphere. The inset: SAED pattern of graphene oxide nanosheets.

indicated by the emergence of a black color. The Pd complex doped mesophase remains colorless and upon photoirradiation turns to a black gel after 12 hours but remains translucent (Fig. 1 inset). In fact, immediately after photoirradiation, the hexagonal mesophase turns into a faint black gel but the darkness of the gel increases with progress of the reduction of Pd(II).

After photoreduction of the Pd complex within the hexagonal mesophases, it is important to ensure the stability of the hexagonal mesophases in order to understand the effect of confinement. The hexagonal phases are birefringent and exhibit characteristic textures between crossed polarizing windows when the surfactant cylinders are parallel to the walls of the observation cell. The polarized optical microscopy image (Fig. S2a–d†) demonstrates that the presence of the Pd complex (Fig. S2b†) and the photo-induced chemical transformation (Fig. S2c and d†) do not affect the birefringent nature of the gels or their texture. After photoreduction of the Pd complex, the hexagonal LC phase shows a large degree of preservation of the birefringent pattern indicative of their stability. The photoreduction of the Pd complex in hexagonal mesophases leads to Pd nanostructures as shown in Fig. 2.

The as-prepared Pd nanostructures assembled together as prolate ellipsoid-like structures composed of a self-assembly of small Pd nanoparticles (NPs) of 3–4 nm in size (Fig. 2a–c). A magnified image (Fig. 2b and c) reveals that the nanoparticles have a narrow size distribution and are well dispersed. It can be clearly seen that the prolate ellipsoid-like nanostructures are formed by the agglomeration of smaller Pd nanoparticles. It can be assumed that after template removal, the nanoparticles are close to each other and their inter-particle interaction may contribute to the assembled structure. The selected area electron diffraction (SAED) pattern recorded from one of the Pd nanostructures (inset of Fig. 2a) shows diffraction rings corresponding to various facets of the cubic (fcc) crystal structure of palladium. The HRTEM image (Fig. 2d) further confirms that each nanostructure is composed of many single crystalline grains (see the white dashed circles in Fig. 2d with their crystallographic orientations). The inter-planar distance in the lattice fringes of one domain is measured to be 0.22 nm (inset), which corresponds to the (111) planes of metallic Pd.

The XRD pattern of the typical product is presented in Fig. 2e. The broad diffraction peaks are present at $2\theta = 40.6^\circ$, 46.6°, 68.4°, 82° and 87° and can be indexed as the (111), (200), (220), (311) and (222) facets of face-centered cubic (fcc) Pd (JCPDS no. 05-0681), respectively. This indicates that the Pd NPs have a high purity and crystallinity. Both the XRD and SAED patterns demonstrate that the Pd nanostructures are well crystallized. Time evolution of Pd nanostructures implied that small Pd particles were generated at the early stage of the reaction by fast reduction *via* the particle attachment growth mechanism (Fig. S3†). The dendritic Pd nanostructures seem to be assembled from many small Pd NPs in the range of 3–4 nm.

Fig. 2e shows the TEM image of reduced graphene oxides (RGO) which exhibit typical wrinkled and paper-like sheet morphologies with a mixture of single and few-layer graphene nanosheets. The observed corrugation and scrolling of sheets is the intrinsic nature of graphene, which may originate from the thermodynamic stabilization of the 2D membrane structures *via* bending. Fig. 2e inset depicts the SAED pattern of RGO, which clearly demonstrates a highly crystalline structure. The six membered inner rings originate from the [100] plane, while the six brilliant points relate to the [110] diffractions, clearly confirming that the resulting RGO has been restored into the hexagonal graphene framework (images at higher resolutions and layered morphologies are shown in Fig. S4†).[61] The ability to produce graphene nanosheets with a scalable, clean (without using any chemical reducing agent) and low-cost approach should take us a step closer to real-world applications of graphene.

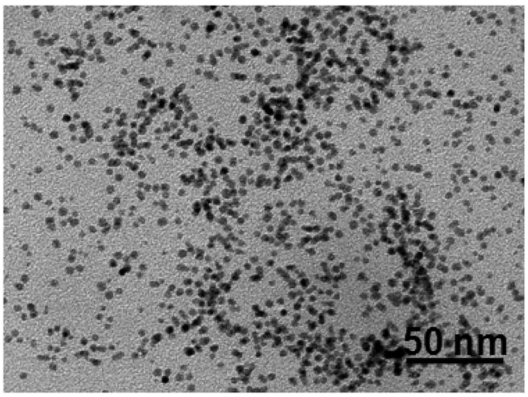

Fig. 3 TEM micrograph of Pd nanoparticles obtained from the micellar solution of CPCl containing $Pd(NH_3)_4Cl_2$ ([CPCl]/[Pd] = 14) at 12 h photo-irradiation.

The control experiment was carried out in micellar solutions formed by CPCl containing $Pd(NH_3)_4Cl_2$ (with the same ratio [CPCl]/[Pd] = 14). The photoreduction of the Pd complex leads in this case to the formation of small and spherical dispersed nanoparticles of 3–5 nm (Fig. 3). Additionally, Pd complex doped hexagonal mesophases were kept in the dark for several days but there was no sign of evolution of Pd(0). Under UV irradiation, Pd(II) is reduced at the oil–water interface.[33,62] Initially, nuclei are formed and then they tend to aggregate to form bigger particles or successive reduction of Pd(II) may result in its adsorption on the surface of preformed particles. In this regard, surfactant molecules protect the metal clusters and control the aggregation *via* hydrophobic chain mediated electrostatic repulsion and steric hindrance. However, it is difficult to convey the exact mechanism of formation of prolate ellipsoid-like structures within the hexagonal mesophases.

The confined geometry of mesophases is certainly involved in directing the nanoparticle growth leading to these assembled Pd nanostructures. The hexagonal mesophases consist of infinite nonpolar tubes organized on a hexagonal lattice with surfactants at the interface of the tubes in a continuous aqueous salt solution. It has been demonstrated that the suitable correct adjustment between cyclohexane and the ionic force of the aqueous solution by the addition of a salt allowed the diameter of the nonpolar cylinders to be tuned over 1 order of magnitude (from 3 to 30 nm), while the distance between adjacent

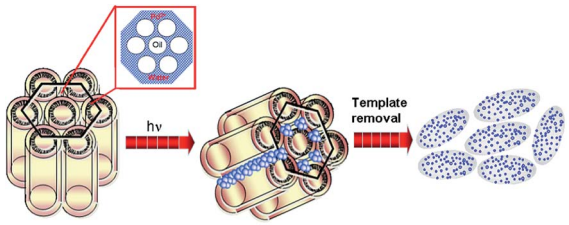

Scheme 1 Schematic representation of the light induced synthesis of Pd nanostructures in hexagonal mesophases.

cylinders is kept small and nearly constant (about 3 nm).[21,32] Here, we demonstrate that the confined aqueous phase can be used as nanoreactors for the preparation of Pd nanostructures as shown in Scheme 1.

In order to shed light on the mechanism of formation of Pd nanostructures within the confined geometry of hexagonal mesophases, we studied the solvation dynamics in the water surface and hydrophobic region of the oil tube of the LC followed by doping with a solvation probe such as coumarin 500 (C500) and 4-(dicyanomethylene)-2-methyl-6-(*p*-dimethylaminostyryl)-4*H*-pyran (DCM) respectively. The picosecond resolved fluorescence transients of C500 and DCM in mesophases across the emission wavelengths are shown in Fig. 4a and b respectively. An ultrafast decay component in the blue end is eventually converted into a rise component of similar time constant in both the cases. The observation is consistent with the solvation probe C500 and DCM in the corresponding medium.[63,64] Fig. 4c and d show the constructed time-resolved emission spectra (TRES) of C500 and DCM with a spectral shift of 1790 and 2268 cm^{-1} respectively, in a 1.5 ns time window, which indicate that both probes are stabilized by the corresponding immediate solvent molecules in the excited state. To determine the water relaxation dynamics within the hexagonal mesophases, we composed solvation correlation functions [$C(t)$] for both probes C500 and DCM and fitted with the bi-exponential decay function as shown in Fig. 4e and f.

For C500, the decay time constants are 20 ps (92%) and 319 ps (8%) and for DCM, the obtained time constants are 170 ps (96%) and 1.49 ns (4%). The slower water dynamics for the hydrophobic DCM molecule is associated with the confinement of DCM in the hydrophobic region (oil tube) of the hexagonal mesophases in comparison to less hydrophobic C500 in the oil–water interface. Hence, more water can access the C500 probe in the excited state compared to DCM. In order to investigate the location and physical movement of C500 and DCM molecules within the LC during the course of solvent relaxation, we have measured the fluorescence anisotropy of the probe molecules as shown in the insets of Fig. 4e and f. The fluorescence anisotropy decays show that the rotational relaxation time constants of C500 and DCM in the liquid crystal are 653 ps and 325 ps respectively. The observed faster rotational time constants in the case of DCM are consistent with the fact that DCM resides on the more compact oil phase while on the other hand C500 is more flexible on the oil–water interface. Hence, we can conclude that due to the hydrophobicity as well as the compact nature of the oil phase, reduction of the Pd complex takes place in the aqueous phase; consequently, the nanoparticles are formed in the oil–water interface within the mesophases as proposed in Scheme 1.

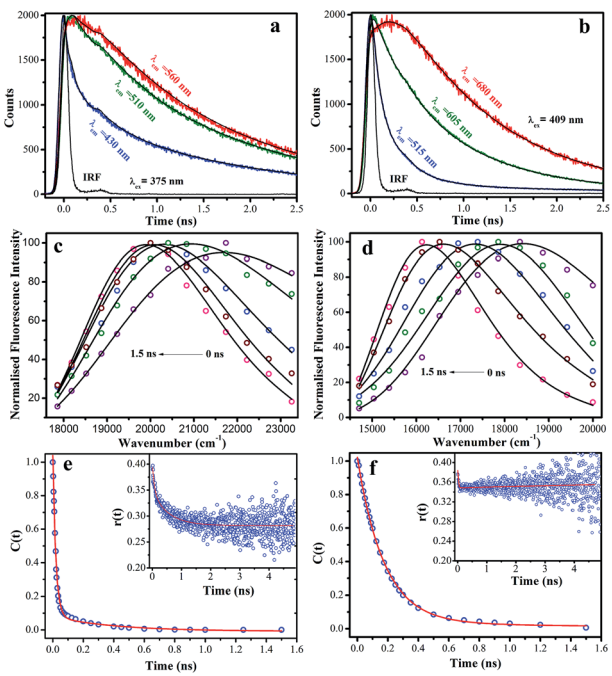

Fig. 4 Picosecond resolved fluorescence transients of (a) C500 and (b) DCM in three representative detection wavelengths across the emission spectrum in hexagonal mesophases. Time dependent emission spectra of (c) C500 and (d) DCM in the liquid crystal are shown. Plot of solvation correlation functions against time for (e) C500 and (f) DCM are shown. Insets depict the picosecond fluorescence anisotropy decays of C500 and DCM.

3.1 Electrochemical behavior

As Pd-modified electrodes were demonstrated to be very active for ethanol electrooxidation in the alkaline medium, EOR was selected for electrocatalytic studies.[10,15,16,65,66] Fig. 5a and b depict the cyclic voltammogram (CV) of Pd-Nafion (green solid line) and Pd/RGO–Nafion (blue solid line) in pure 1 M NaOH and the voltammetric pattern associated with the characteristic feature of Pd electrodes which is consistent with earlier reports.[15,16,43] The Pd nanostructures embedded in a proton conducting phase, Nafion and RGO–Nafion matrix, were used as the catalyst for the electrocatalytic oxidation of ethanol in an alkaline medium. Fig. 5a and b show superposition of the first cyclic voltammogram (black solid line curve) and the 100th cycle (red solid line curve) of Pd/Nafion and Pd/RGO–Nafion run in 1 M NaOH containing 1 M EtOH at a scan rate of 50 mV s^{-1}.

The voltammetric pattern is represented by two well-defined current peaks, one on the forward and the other on the reverse potential scans. The peak in the positive-going sweep corresponds to ethanol oxidation activity, while the peak in the reverse sweep arises due to oxidation of both freshly adsorbed ethanol and adsorbed carbonaceous species formed before Pd–O blocking.[67]

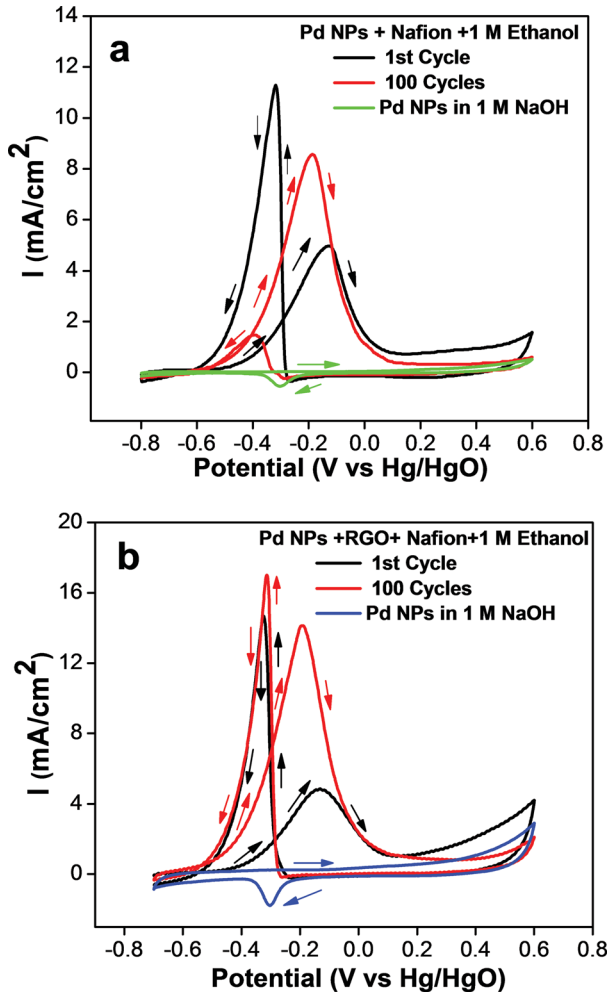

Fig. 5 (a) Cyclic voltammograms of Pd NPs/Nafion in 1 M NaOH (green solid line), superposition of the first (black solid line curve) and the 100th (red solid line curve) cyclic voltammetric runs associated with the electrocatalytic oxidation of 1 M EtOH in 1 M NaOH. (b) Cyclic voltammograms of Pd NPs/RGO–Nafion in 1 M NaOH (blue solid line), superposition of the first (black solid line curve) and the 100th (red solid line curve) cyclic voltammetric runs associated with the electrocatalytic oxidation of 1 M EtOH in 1 M NaOH. The working electrode was a glassy carbon disk modified with the Pd nanostructures. The reference electrode was an Hg/HgO (1 M KOH) electrode. The scan rate was 50 mV s^{-1}.

The forward scan peak current is related to the oxidation of freshly chemisorbed species generated from alcohol adsorption. The initial increment of current with the number of triangular potential sweeps may be attributed to the generation of Pd–OH on the surface after each scan and development of channels of electron collection by rearrangement of the materials at the surface.[42] The oxygen desorption method is applicable to evaluate the electrochemically active surface area (ECSA) of Pd. The mass normalized ESCA was calculated for the two electrodes by computing the area under the cathodic peaks corresponding to the reaction of the Pd oxide monolayers. The data presented (within parentheses) reveal that ECSA of Pd/RGO–Nafion (192 m^2 g^{-1}) is about 4.6 times greater than that of the Pd/Nafion electrode (40 m^2 g^{-1}). This signifies that the former electrode is more exposed to and available in the solvent environment for undergoing the reactions and hence shows increased surface area induced catalytic effect. The peak current and onset potential of the faradaic current (E_{onset}) on the forward scan indicate the electrocatalytic activity of the catalyst for EOR. The main quantitative parameters measured from these two voltammograms have been tabulated (Table 1). It can be clearly seen from Table 1 that the electroactivity (considering current per cm^2 of real area) of Pd/Nafion-RGO is higher than that of the Pd/Nafion electrode. During the potential cycles, the E_{onset} shifts to a more negative potential (from −534 mV at the 1st cycle to −590 mV after 100 cycles, Table 1). It has to be noted that the stable cycle and 100 cycles are similar and used for further calculation of electrochemical parameters. A negative shift of E_{onset} underscores the enhancement in the kinetics of ethanol oxidation. Upon cycling, the peak current density is also modified: the forward anodic peak current density (I_f) increased from 4.93 mA cm^{-2} to 8.55 mA cm^{-2} whereas the backward anodic peak current density (I_b) decreased from 11.20 mA cm^{-2} to 1.43 mA cm^{-2}, leading to an increase of the ratio I_f/I_b from 0.44 to 5.98. This observation indicates that the catalyst is not lost during the reaction and also shows a relatively significant increase of electro-catalytic activity of the electrode material toward EOR during cycling. Indeed, a high I_f/I_b ratio indicates efficient oxidation of alcohol during the forward anodic scan, with little accumulation of carbonaceous residues. Thus it measures the tolerance power towards carbonaceous poisons and represents the capability of the electrode to remove the poisons either by possible chemical or electrochemical reactions occurring in the system.

Here the ratio of Pd/RGO–Nafion (0.83) is much smaller than that of Pd/Nafion (5.98). This is possibly because the spectroscopically determined intermediates, like Pd–CH_3, PdCH_3CO, Pd–H *etc.*, are eliminated from the surface both by chemical and electrochemical reactions leading to the opening of a fresh

Table 1 Comparison of the electrochemical performance of Pd nanoparticle catalysts with Nafion and reduced graphene oxide nanosheets modified Nafion as supports for the oxidation of ethanol. The main characteristics were measured from cyclic voltammograms associated with the electrocatalytic oxidation of 1 M EtOH in 1 M NaOH. The working electrode was a glassy carbon disc modified with the Pd nanostructures. The reference electrode was an Hg/HgO (1 M NaOH) electrode. The scan rate was 50 mV s^{-1}. The current density refers to the geometric area of the glassy carbon support

Electrodes (after 100 cycles)	I_f (mA cm^{-2})	I_b (mA cm^{-2})	I_f/I_b	E_{onset} (mV)	I_f (mA cm^{-2}) mg^{-1}	I_b (mA cm^{-2}) mg^{-1}
Pd/Nafion	8.55	1.43	5.98	−590	1745	292
Pd/RGO–Nafion	14.22	17.08	0.83	−622	5925	7166

Table 2 Comparison of the electrochemical performance of Pd nanostructured electrocatalysts for ethanol oxidation

Electrode	E_{onset}, mV/SCE	E_f, mV/SCE	E_b, mV/SCE	I_f, mA cm^{-2}	I_f, mA cm^{-2} mg^{-1} of Pd	Reference
Pd/Nafion	−590	−185	−382	8.55	1745	This work
Pd/RGO–Nafion	−622	−186	−312	14.22	5925	This work
Commercial Pd black catalyst	−550	∼−200	∼−301	0.65	—	8
Tetrahedral Pd nanocrystals	−590	−219	∼−305	3.83	—	8
Pd/Nf–graphene	−600	—	—	0.56		2
C–Pd nanoballs/Nafion	−550	−151	−296	—	—	16
Pd nanowires/Nafion	−664	−166	−278	—	1327	15
CNT–Pd/Nafion	−564	−242	−451	—	364	37
CNT–Pd/Nafion	−670	−245	−332	—	3540	37
C–Pd	−680	−209	∼−310	—	63	63
C–Pd	−579	−219	∼−360	—	42	64
C–Pd	−619	−203	∼−330	—	85	64

metal surface. Since the rate of formation of these intermediates is greater for the electrode for which the peak current density is larger, the rate of elimination of these intermediates from the surface is also greater.[44,68] If Pd–CH_3 or Pd–H is removed by an electrochemical oxidation reaction the following reactions would take place:

$$Pd–CH_3 + 9OH^- = Pd + CO_3^{2-} + 6\,H_2O + 7e^- \quad (1)$$

$$Pd–H + OH^- = Pd + H_2O + e^- \quad (2)$$

In contrast, if they are removed chemically, the following reactions would occur:

$$Pd–CH_3 + Pd–CH_3 = 2Pd + C_2H_6 \quad (3)$$

$$Pd–CH_3 + Pd–H = 2Pd + CH_4 \quad (4)$$

The loss in I_f, which corresponds to both faster dehydrogenation and slower decarbonaceous oxidation, is more than that in I_b which mainly occurs due to surface-adsorbed carbonaceous oxidation. Thus the ratio I_f/I_b is much smaller for Pd/RGO–Nafion than Pd/Nafion. This type of increased I_f/I_b ratio for better performance is a general phenomenon as observed in our previous study.[44] However, the increment in the forward anodic peak current density with respect to the backward anodic peak current density was evaluated from potentiostatic experiments to identify the catalyst's tolerance to carbonaceous species accumulation.[15] Similar results have also been obtained for Pd-nanowires and palladium/gold nanostructures and such improvement in modified electrode characteristics might be attributed to some reorganization of the surface film[10,43] or to a gradual cleaning of the surfactant that remains after the synthesis.[15] Similar electrochemical behavior upon cycling was observed with Pd NPs supported by RGO–Nafion (Pd/RGO–Nafion), assuming that the particular behavior is inherent to metallic NPs. We verified the contribution of control RGO nanosheets during EOR. Fig. S5† shows the cyclic voltammograms for RGO nanosheets before and after addition of EtOH. However, the presence of RGO in combination with Nafion as a support for Pd NPs influenced the values of E_{onset}, the measured current density and the I_f/I_b ratio (Table 1). The onset of ethanol oxidation occurs at −0.590 V for Pd/Nafion whereas it is −0.622 V for Pd/RGO–Nafion suggesting that the electrocatalytic activity towards ethanol oxidation occurs more favorably in Pd/RGO–Nafion than in Pd/Nafion. It has been observed that in the first cycle, the peak current densities increased for both the forward and the backward scans and in contrast to Pd/Nafion, strikingly, backward current density increases after 100 cycles (Fig. 5b). According to the values extracted from the voltammograms, Pd NPs in Nafion were the less active system compared to those in the RGO–Nafion support, but they exhibited the best I_f/I_b ratio. An explanation for the high I_f/I_b ratio of Pd/Nafion could be that the nature of the support RGO influences the adsorbed organic functions at the surface of the Pd NPs. The forward peak current density of Pd/Nafion and Pd/RGO–Nafion was 8.55 and 14.22 mA cm^{-2}, respectively. The forward peak current of the Pd/RGO–Nafion catalyst is 1.66 times that of the Pd/Nafion catalyst. Since loading of the catalyst is different for the electrodes, peak current densities of the CVs

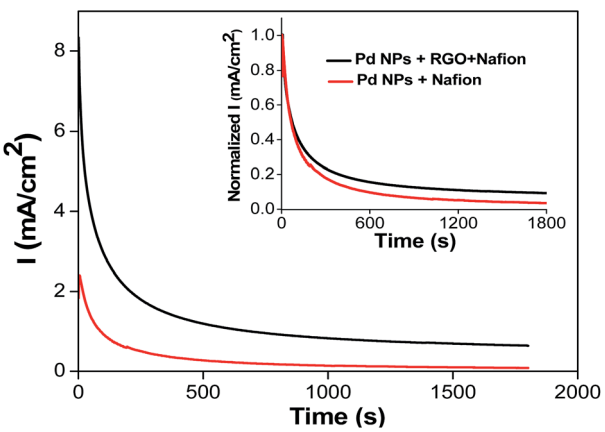

Fig. 6 Chronoamperometric curves for ethanol electrooxidation at −0.30 V *vs.* Hg/HgO on a glassy carbon electrode modified with Pd/Nafion (black curve) and Pd/RGO–Nafion (red curve). The solution used was 1 M NaOH + 1 M EtOH. Inset: comparison of the chronoamperometric response of Pd/Nafion and Pd/RGO–Nafion at normalized current (*I*).

were expressed by dividing current densities (mA cm^{-2}) by the mass of Pd adsorbed per unit area of the surface (mg^{-1} of catalyst) as shown in Table 1.The influence of the high surface area of RGO as the support (Table 1) clearly highlights that the RGO–Nafion support exhibited higher current density.[69] Comparison of the electrochemical performance of the present Pd nanostructure with other Pd based nanostructures under comparable reaction conditions is presented in Table 2. Interestingly, the superiority of Pd/RGO–Nafion in terms of current density (7166 mA cm^{-2} mg^{-1}) is obvious, being nearly 4.4 times higher than that of previously reported Pd nanowires (1327 mA cm^{-2} mg^{-1}) synthesized in hexagonal mesophases as shown in Table 2.[15] In fact, the Pd/RGO–Nafion catalyst has superior catalytic activity with high energy density among these Pd catalysts. This may be due to the synergistic effect of assembled Pd nanoparticles and reduced graphene oxide nanosheets that can efficiently promote the breaking of the C–C bond of ethanol and enhance its oxidation. In contrast to the Pd assembly, the Pd NPs synthesized within micelles are not active due to the presence of surfactant molecules which limit the accessibility of the Pd electrocatalyst on the electrode.

The catalyst stability as a function of time is also important for its practical application in direct ethanol fuel cells. The stability of the catalytic performance was then investigated by chronoamperometric (CA) measurements where the current density–time (*I vs. t*) curves at constant potentials were recorded as shown in Fig. 6.

The CA experiments were carried out in 1 M NaOH with 1 M ethanol solution under a constant potential of 0.3 V for 1600 s. In the first several minutes, both catalysts exhibited a pronounced current decay, which could be caused by the accumulation of poisonous intermediates.[70] The current density decayed in the first 500 s and attained a steady state thereafter, indicating that these Pd NPs form very stable film on the glassy carbon electrode surface and also exhibit stable electrocatalytic performance towards EOR. After 500 s, the order of activity in the CA tests was similar to the activity order in the CV measurements: Pd/RGO–Nafion catalyst exhibited the highest limiting as well as initial current, showing higher activity than the Pd/Nafion catalysts. Moreover, Pd/RGO–Nafion exhibits a lower degradation rate during the progress of the reaction, which demonstrates its improved stability for ethanol electrooxidation. The enhanced EOR activity and stability for the Pd/RGO–Nafion electrocatalyst compared to Pd/Nafion are probably related to the surface structure and properties of the reduced graphene oxide nanosheets. The chronoamperometric response confirms that the RGO nanosheets help in the effective dispersion of the Pd NPs, facilitating an easier access of ethanol molecules to the catalytic sites. Additionally, the RGO nanosheets containing holes, oxygen, carbon vacancies and defects, which are generated due to partial oxidation, produce sheets with graphitic domains. This may efficiently introduce chemically active sites for use in catalytic reactions and also act as anchoring sites for deposition of metal NPs.[49,71] Furthermore, it is also beneficial to prevent the metal nanoclusters from coalescing because of the homogeneous dispersion of the Pd NPs on the support and consequently the accessibility of the metal catalyst during the electrocatalytic reaction increases.[72] Hence, the addition of reduced GO nanosheets as a support could remarkably improve the stability of the Pd nanostructure for EOR, which is crucial for a practical catalyst.

4. Conclusions

In summary, we have successfully developed a facile and reproducible method for the high-yield synthesis of assembled Pd nanostructures in hexagonal mesophases by photoreduction. The as-prepared electrocatalysts supported with RGO nanosheets exhibit dramatically enhanced activity and stability for ethanol electrooxidation in alkaline conditions, demonstrating that they can be used as effective electrocatalysts for direct ethanol fuel cells. Hence, the RGO–Nafion support can eventually affect the overall quality of the electro-catalytic activity of the Pd nanostructure with high current density and more negative onset potentials of the faradaic current which is also supported by the 4.6 times higher ECSA in comparison with Nafion alone. In light of the important role of nanostructures in catalysis and their facile synthesis process, the as-synthesized catalysts may also find suitable applications in other fuel cells relevant reactions, such as formic acid oxidation, methanol oxidation and oxygen reduction reaction. The coupling of graphene oxide nanosheets with metal nanostructures leads to superior activity. The use of graphene nanosheets synthesized by a scalable, clean approach without using any chemical reducing agent *via* a low-cost approach may encourage real-world applications in the field of fuel cells. Moreover, the electrochemical performance of Pd based materials is strongly dependent on individual components and their interactions with each other. Hence, further studies are required to understand the underlying complex interactions between the Pd catalyst and graphene based support. Finally, exploration of novel Pd assembled nanostructures supported with graphene oxide nanosheets and Nafion can be extended to design other advanced materials for a promising anode catalyst in DEFCs.

Acknowledgements

S.G. acknowledges Marie Curie Cofund, RBUCE-UP (Research Based University Chairs of Excellence of Paris) and PRES UniverSud Paris for financial support. P.K. and S.C. thank the Council of Scientific and Industrial Research (CSIR, India) for fellowships. S.K.P. thanks the Department of Science and Technology (DST, India) for financial grants. The authors gratefully acknowledge C'Nano Ile de France and Université Paris-Sud (ERM project) for financial support for the Cobalt-60 panoramic gamma source.

Notes and references

1 A. S. Arico, P. Bruce, B. Scrosati, J.-M. Tarascon and W. van Schalkwijk, *Nat. Mater.*, 2005, **4**, 366–377.
2 Q. Zhang, E. Uchaker, S. L. Candelaria and G. Cao, *Chem. Soc. Rev.*, 2013, **42**, 3127–3171.

3 P. Kar, S. Sardar, E. Alarousu, J. Sun, Z. S. Seddigi, S. A. Ahmed, E. Y. Danish, O. F. Mohammed and S. K. Pal, *Chem.–Eur. J.*, 2014, **20**, 10475–10483.

4 X. Cheng, Z. Shi, N. Glass, L. Zhang, J. Zhang, D. Song, Z.-S. Liu, H. Wang and J. Shen, *J. Power Sources*, 2007, **165**, 739–756.

5 E. Christoffersen, P. Liu, A. Ruban, H. L. Skriver and J. K. Nørskov, *J. Catal.*, 2001, **199**, 123–131.

6 C. Bianchini and P. K. Shen, *Chem. Rev.*, 2009, **109**, 4183–4206.

7 P. S. Roy, J. Bagchi and S. K. Bhattacharya, *Catal. Sci. Technol.*, 2012, **2**, 2302–2310.

8 N. Tian, Z.-Y. Zhou, N.-F. Yu, L.-Y. Wang and S.-G. Sun, *J. Am. Chem. Soc.*, 2010, **132**, 7580–7581.

9 X. Huang, Y. Li, Y. Li, H. Zhou, X. Duan and Y. Huang, *Nano Lett.*, 2012, **12**, 4265–4270.

10 F. Ksar, L. Ramos, B. Keita, L. Nadjo, P. Beaunier and H. Remita, *Chem. Mater.*, 2009, **21**, 3677–3683.

11 C. Koenigsmann, A. C. Santulli, E. Sutter and S. S. Wong, *ACS Nano*, 2011, **5**, 7471–7487.

12 X. Huang, S. Tang, X. Mu, Y. Dai, G. Chen, Z. Zhou, F. Ruan, Z. Yang and N. Zheng, *Nat. Nanotechnol.*, 2011, **6**, 28–32.

13 P. S. Roy and S. K. Bhattacharya, *Catal. Sci. Technol.*, 2013, **3**, 1314–1323.

14 H. Zhang, M. Jin, Y. Xiong, B. Lim and Y. Xia, *Acc. Chem. Res.*, 2012, **46**, 1783–1794.

15 F. Ksar, G. Surendran, L. Ramos, B. Keita, L. Nadjo, E. Prouzet, P. Beaunier, A. Hagège, F. Audonnet and H. Remita, *Chem. Mater.*, 2009, **21**, 1612–1617.

16 G. Surendran, F. Ksar, L. Ramos, B. Keita, L. Nadjo, E. Prouzet, P. Beaunier, P. Dieudonné, F. Audonnet and H. Remita, *J. Phys. Chem. C*, 2008, **112**, 10740–10744.

17 L.-F. Zhang, S.-L. Zhong and A.-W. Xu, *Angew. Chem., Int. Ed.*, 2013, **52**, 645–649.

18 S. Guo, S. Dong and E. Wang, *Energy Environ. Sci.*, 2010, **3**, 1307–1310.

19 P. K. Shen and C. Xu, *Electrochem. Commun.*, 2006, **8**, 184–188.

20 T. Hegmann, H. Qi and V. Marx, *J. Inorg. Organomet. Polym.*, 2007, **17**, 483–508.

21 G. Surendran, G. Apostolescu, M. Tokumoto, E. Prouzet, L. Ramos, P. Beaunier, P. J. Kooyman, A. Etcheberry and H. Remita, *Small*, 2005, **1**, 964–967.

22 K. Kanie and T. Sugimoto, *J. Am. Chem. Soc.*, 2003, **125**, 10518–10519.

23 S. Kubo, R. Taguchi, S. Hadano, M. Narita, O. Watanabe, T. Iyoda and M. Nakagawa, *ACS Appl. Mater. Interfaces*, 2013, **6**, 811–818.

24 J. Mirzaei, M. Urbanski, H.-S. Kitzerow and T. Hegmann, *ChemPhysChem*, 2014, **15**, 1381–1394.

25 V. J. Anderson, E. M. Terentjev, S. P. Meeker, J. Crain and W. C. K. Poon, *Eur. Phys. J. E*, 2001, **4**, 11–20.

26 P. G. Petrov and E. M. Terentjev, *Langmuir*, 2001, **17**, 2942–2949.

27 S. P. Meeker, W. C. K. Poon, J. Crain and E. M. Terentjev, *Phys. Rev. E: Stat. Phys., Plasmas, Fluids, Relat. Interdiscip. Top.*, 2000, **61**, R6083–R6086.

28 G. S. Attard, P. N. Bartlett, N. R. B. Coleman, J. M. Elliott, J. R. Owen and J. H. Wang, *Science*, 1997, **278**, 838–840.

29 G. S. Attard, J. M. Corker, C. G. Göltner, S. Henke and R. H. Templer, *Angew. Chem., Int. Ed.*, 1997, **36**, 1315–1317.

30 A. Lehoux, L. Ramos, P. Beaunier, D. B. Uribe, P. Dieudonné, F. Audonnet, A. Etcheberry, M. José-Yacaman and H. Remita, *Adv. Funct. Mater.*, 2012, **22**, 4900–4908.

31 E. Pena dos Santos, M. S. Tokumoto, G. Surendran, H. Remita, C. Bourgaux, P. Dieudonné, E. Prouzet and L. Ramos, *Langmuir*, 2005, **21**, 4362–4369.

32 G. Surendran, M. S. Tokumoto, E. Pena dos Santos, H. Remita, L. Ramos, P. J. Kooyman, C. V. Santilli, C. Bourgaux, P. Dieudonné and E. Prouzet, *Chem. Mater.*, 2005, **17**, 1505–1514.

33 T. Redjala, G. Apostolecu, P. Beaunier, M. Mostafavi, A. Etcheberry, D. Uzio, C. Thomazeau and H. Remita, *New J. Chem.*, 2008, **32**, 1403–1408.

34 P. F. Siril, L. Ramos, P. Beaunier, P. Archirel, A. Etcheberry and H. Remita, *Chem. Mater.*, 2009, **21**, 5170–5175.

35 S. Ghosh, N. A. Kouamé, L. Ramos, S. Remita, A. Dazzi, A. Deniset-Besseau, P. Beaunier, F. Goubard, P. H. Aubert and H. Remita, *Nat. Mater.*, 2015, DOI: 10.1038/nmat4220.

36 S. Ghosh, H. Remita, L. Ramos, A. Dazzi, A. Deniset-Besseau, P. Beaunier, F. Goubard, P.-H. Aubert, F. Brisset and S. Remita, *New J. Chem.*, 2014, **38**, 1106–1115.

37 N. Mackiewicz, G. Surendran, H. Remita, B. Keita, G. Zhang, L. Nadjo, A. Hagège, E. Doris and C. Mioskowski, *J. Am. Chem. Soc.*, 2008, **130**, 8110–8111.

38 R. Krishna, E. Titus, O. Okhay, J. C. Gil, J. Ventura, E. V. Ramana and J. J. A. Gracio, *Int. J. Electrochem. Sci.*, 2014, **9**, 4054–4069.

39 H. T. Zheng, Y. Li, S. Chen and P. K. Shen, *J. Power Sources*, 2006, **163**, 371–375.

40 P. Kanninen, M. Borghei, V. Ruiz, E. I. Kauppinen and T. Kallio, *Int. J. Hydrogen Energy*, 2012, **37**, 19082–19091.

41 M. A. Newton, C. Belver-Coldeira, A. Martinez-Arias and M. Fernandez-Garcia, *Nat. Mater.*, 2007, **6**, 528–532.

42 H. L. Xin, J. A. Mundy, Z. Liu, R. Cabezas, R. Hovden, L. F. Kourkoutis, J. Zhang, N. P. Subramanian, R. Makharia, F. T. Wagner and D. A. Muller, *Nano Lett.*, 2011, **12**, 490–497.

43 S. Ghosh, A.-L. Teillout, D. Floresyona, P. de Oliveira, A. Hagège and H. Remita, *Int. J. Hydrogen Energy*, 2015, **40**, 4951–4959.

44 P. Mukherjee, P. S. Roy, K. Mandal, D. Bhattacharjee, S. Dasgupta and S. K. Bhattacharya, *Electrochim. Acta*, 2015, **154**, 447–455.

45 Y. Zhao, L. Zhan, J. Tian, S. Nie and Z. Ning, *Electrochim. Acta*, 2011, **56**, 1967–1972.

46 E. Antolini, *Appl. Catal., B*, 2012, **123–124**, 52–68.

47 Y. Li, H. Wang, L. Xie, Y. Liang, G. Hong and H. Dai, *J. Am. Chem. Soc.*, 2011, **133**, 7296–7299.

48 Y. Liang, Y. Li, H. Wang, J. Zhou, J. Wang, T. Regier and H. Dai, *Nat. Mater.*, 2011, **10**, 780–786.

49 E. Yoo, T. Okata, T. Akita, M. Kohyama, J. Nakamura and I. Honma, *Nano Lett.*, 2009, **9**, 2255–2259.

50 C. Huang, C. Li and G. Shi, *Energy Environ. Sci.*, 2012, **5**, 8848–8868.
51 S. Stankovich, D. A. Dikin, G. H. B. Dommett, K. M. Kohlhaas, E. J. Zimney, E. A. Stach, R. D. Piner, S. T. Nguyen and R. S. Ruoff, *Nature*, 2006, **442**, 282–286.
52 W. S. Hummers and R. E. Offeman, *J. Am. Chem. Soc.*, 1958, **80**, 1339.
53 D. Li, M. B. Muller, S. Gilje, R. B. Kaner and G. G. Wallace, *Nat. Nanotechnol.*, 2008, **3**, 101–105.
54 M. L. Horng, J. A. Gardecki, A. Papazyan and M. Maroncelli, *J. Phys. Chem.*, 1995, **99**, 17311–17337.
55 S. Batabyal, T. Mondol, S. Choudhury, A. Mazumder and S. K. Pal, *Biochimie*, 2013, **95**, 2168–2176.
56 J. Bagchi and S. K. Bhattacharya, *J. Power Sources*, 2007, **163**, 661–670.
57 M. Manfait, A. J. P. Alix and C. Kappenstein, *Inorg. Chim. Acta*, 1981, **50**, 147–152.
58 K. H. S. Kung and K. F. Hayes, *Langmuir*, 1993, **9**, 263–267.
59 K. R. Gopidas, J. K. Whitesell and M. A. Fox, *Nano Lett.*, 2003, **3**, 1757–1760.
60 M. N. Nadagouda and R. S. Varma, *Green Chem.*, 2008, **10**, 859–862.
61 G. Wang, J. Yang, J. Park, X. Gou, B. Wang, H. Liu and J. Yao, *J. Phys. Chem. C*, 2008, **112**, 8192–8195.
62 F. Dehouche, P. Archirel, H. Remita, N. Brodie-Linder and A. Traverse, *RSC Adv.*, 2012, **2**, 6686–6694.
63 S. Choudhury, S. Batabyal, T. Mondol, D. Sao, P. Lemmens and S. K. Pal, *Chem.–Asian J.*, 2014, **9**, 1395–1402.
64 R. Sarkar, A. K. Shaw, M. Ghosh and S. K. Pal, *J. Photochem. Photobiol., B*, 2006, **83**, 213–222.
65 C. Xu, P. K. Shen and Y. Liu, *J. Power Sources*, 2007, **164**, 527–531.
66 M. Grdeń, M. Łukaszewski, G. Jerkiewicz and A. Czerwiński, *Electrochim. Acta*, 2008, **53**, 7583–7598.
67 R. Mancharan and J. B. Goodenough, *J. Mater. Chem.*, 1992, **2**, 875–887.
68 K. Mandal, D. Bhattacharjee, P. S. Roy, S. K. Bhattacharya and S. Dasgupta, *Appl. Catal., A*, 2015, **492**, 100–106.
69 X. Yang, Q. Yang, J. Xu and C.-S. Lee, *J. Mater. Chem.*, 2012, **22**, 8057–8062.
70 A. Kabbabi, R. Faure, R. Durand, B. Beden, F. Hahn, J. M. Leger and C. Lamy, *J. Electroanal. Chem.*, 1998, **444**, 41–53.
71 K. Erickson, R. Erni, Z. Lee, N. Alem, W. Gannett and A. Zettl, *Adv. Mater.*, 2010, **22**, 4467–4472.
72 G. Prieto, J. Zečević, H. Friedrich, K. P. de Jong and P. E. de Jongh, *Nat. Mater.*, 2013, **12**, 34–39.